Biophysical Journal
Article

Biophysical Society

Effect of Ceramide Tail Length on the Structure of Model Stratum Corneum Lipid Bilayers

Timothy C. Moore,[1,2] Remco Hartkamp,[1,2] Christopher R. Iacovella,[1,2] Annette L. Bunge,[3] and Clare McCabe[1,2,4,*]
[1]Department of Chemical and Biomolecular Engineering and [2]Multiscale Modeling and Simulation Center, Vanderbilt University, Nashville, Tennessee; [3]Department of Chemical and Biological Engineering, Colorado School of Mines, Golden, Colorado; and [4]Department of Chemistry, Vanderbilt University, Nashville, Tennessee

ABSTRACT Lipid bilayers composed of non-hydroxy sphingosine ceramide (CER NS), cholesterol (CHOL), and free fatty acids (FFAs), which are components of the human skin barrier, are studied via molecular dynamics simulations. Since mixtures of these lipids exist in dense gel phases with little molecular mobility at physiological conditions, care must be taken to ensure that the simulations become decorrelated from the initial conditions. Thus, we propose and validate an equilibration protocol based on simulated tempering, in which the simulation takes a random walk through temperature space, allowing the system to break out of metastable configurations and hence become decorrelated from its initial configuration. After validating the equilibration protocol, which we refer to as random-walk molecular dynamics, the effects of the lipid composition and ceramide tail length on bilayer properties are studied. Systems containing pure CER NS, CER NS + CHOL, and CER NS + CHOL + FFA, with the CER NS fatty acid tail length varied within each CER NS-CHOL-FFA composition, are simulated. The bilayer thickness is found to depend on the structure of the center of the bilayer, which arises as a result of the tail-length asymmetry between the lipids studied. The hydrogen bonding between the lipid headgroups and with water is found to change with the overall lipid composition, but is mostly independent of the CER fatty acid tail length. Subtle differences in the lateral packing of the lipid tails are also found as a function of CER tail length. Overall, these results provide insight into the experimentally observed trend of altered barrier properties in skin systems where there are more CERs with shorter tails present.

INTRODUCTION

The stratum corneum (SC) layer of the skin acts as the main barrier against chemical penetrants and water loss, and is composed of a brick-and-mortar-like arrangement of corneocytes surrounded by a dense, lamellar-structured extracellular lipid matrix. This matrix is a complex mixture primarily composed of an equimolar ratio of ceramides (CERs), which consists of a sphingoid (SPH) base linked to a saturated fatty acid (FA) chain (in most cases), cholesterol (CHOL), and free FAs (FFAs) (1,2). Since the extracellular matrix is widely thought to be the only continuous path for permeation through the SC, proper lipid organization and composition of the lamellar membrane is generally considered crucial for a fully functioning skin barrier. This is supported by the fact that many skin diseases that are characterized by a reduced barrier function also exhibit an altered lipid composition and organization compared to healthy skin (3–6). For example, in the SC of patients who suffer from atopic eczema, a decrease in the average number of CER carbon atoms (3,7), as well as less dense lipid packing and changes in x-ray scattering patterns compared with controls (3), have been observed. Of the two CER tails, reduced CER carbon numbers appear to correspond to a shorter FA tail rather than the sphingoid-base tail (8).

The complex nature of the human SC lipid matrix, featuring 15 unique subclasses of CER lipids and a distribution of CER and FFA chain lengths, has made it challenging to establish the influence of individual lipid species on barrier properties (9). As a result, many experiments have focused on model systems that are composed of simpler mixtures of synthetic lipids whose composition and chain lengths can be precisely controlled (10–21). For example, considering studies of mixtures containing non-hydroxy sphingosine CER (CER NS), CHOL, and FFA, similar to those considered in this work, Mojumdar et al. (14) showed that CHOL is essential to the characteristic phase behavior, and hence barrier properties, of such mixtures, and Školová et al. (19) found that CER-NS-based membranes with

Submitted June 15, 2017, and accepted for publication October 19, 2017.

*Correspondence: c.mccabe@vanderbilt.edu

Remco Hartkamp's present address is Process and Energy Department, Delft University of Technology, CB Delft, the Netherlands.

Editor: Ana-Suncana Smith.

https://doi.org/10.1016/j.bpj.2017.10.031

short acyl chains had increased permeability compared to long-acyl-chain CERs. However, although global structural properties of SC lipid lamellae can be inferred from experiment (e.g., from spectroscopic, scattering, and diffraction data), including information about the localization of molecules across the lamellae, the underlying molecular-level details and in-plane morphology often remain elusive. Furthermore, structural examination using neutron scattering is quite laborious, as many independent systems, each with different deuterated lipids and/or concentrations of deuterated lipids, must be considered to provide a single picture of the structure, and the availability of deuterated lipids may limit the study of specific systems (15,22–24).

Molecular simulation, which offers atomic-level resolution of the entire three-dimensional structure of the lipids at picosecond timescales, has been used to provide a more direct understanding of the molecular interactions in CER-based membranes (25–38), with several studies focusing on the dependence of membrane structure on lipid composition. For example, Das et al. (26) found that CHOL compresses a CER NS bilayer membrane and increases the interdigitation of CER tails in opposing bilayer leaflets. Gupta and Rai (31) simulated a series of lipid bilayers composed of CER NS, CHOL, and FFAs with varying compositions and found that CHOL tends to sit away from the lipid-water interface and increases the thermal stability of the bilayers. The effect of the CER FA tail length on bilayer properties has received considerably less attention. Paloncýová et al. (37) showed that extremely short CER NS FA tails (e.g., four to six carbons) cause a disruption in the headgroup packing of CER NS bilayers, which gives rise to increased permeability; however, the CER NS FA tail lengths considered were much shorter than those found in the SC. More recently, Gupta et al. (30) showed that the permeability of water across pure CER NS bilayers with more biologically relevant tail lengths decreases monotonically with the CER FA tail length, although a structural explanation for this trend was not presented.

Although these computational studies have provided important insight, they also highlight a significant challenge in studying SC lipids with molecular simulation. Specifically, due to the dense packing of the lipid tails, the CER-rich bilayer systems demonstrate negligible molecular diffusion at physiologically relevant temperatures (i.e., 305 K). Even in simulations conducted at elevated temperatures, e.g., 340 K, studies have demonstrated minimal in-plane diffusion of the lipids, even for simulations in excess of 200 ns (32). Additionally, lipids in the gel phase have low rates of rotational relaxation (39). As such, on typical simulation timescales, systems likely exist in metastable configurations that are highly dependent on the initial bilayer structure. Although this may be of little consequence for single-component lipid bilayers, many properties of multicomponent lipid mixtures depend on the in-plane morphology of the individual lipid components, e.g., aggregation versus dispersion of lipid species in the bilayer leaflets; furthermore, the morphology on this size scale is typically not known from experiment (40). Although self-assembled bilayers would, in principle, avoid these problems, it is not currently practical to study the self-assembly of multicomponent bilayers with atomistically detailed models due to the high computational cost and a rough free-energy landscape that could hinder the formation of equilibrium structures; for example, Das et al. (27) found that inverted micelle structures formed in mixtures of three different CERs with CHOL and FFA unless constrained by a wall, in contrast to experiments, where lamellar structures form in bulk. Therefore, since preassembled structures remain more practical for simulating atomistic models, care must be taken that system properties are not biased by the initial configuration, so that reliable conclusions can be made.

Here, molecular dynamics (MD) simulations are used to examine the structural behavior of model SC membranes similar to those studied experimentally (19,41), as well as the role of CER FA tail length and overall lipid composition in structural properties. Specifically, this work focuses on CER NS, as this is the most abundant CER species in the SC and is typically used in model systems. Three sets of systems are studied: pure CER NS, binary mixtures of CER NS and CHOL in 2:1 and 1:1 molar ratios, and equimolar mixtures of CER NS, CHOL, and FFA C24:0. The structure of each of the lipids used in this work is shown in Fig. 1. Mixtures of different-length CERs are used in each set to examine the impact of the CER FA tail length on the systems, which, to date, has not been the focus of any computational studies. To ensure robust results, a random-walk MD (RWMD) algorithm is validated and employed to reduce the dependence of the final bilayer configuration on the assumed initial morphology.

MATERIALS AND METHODS

Model

CER NS consists of a sphingosine base, 18 carbons in length, linked to a saturated FA chain of variable length. Two different FA tail lengths were considered: CER NS C16:0 (Fig. 1 *a*), in which the FA tail is 16 carbons long and approximately equal in length to the sphingosine chain (denoted as equal-length CER NS, or eCER), and CER NS C24:0 (Fig. 1 *b*), in which the FA tail is 24 carbons long, a typical length in the SC (11) (denoted as unequal-length CER NS, or uCER). FFA, when present in this work, is always 24 carbons in length (Fig. 1 *d*), which has been shown to be a useful model for the FFAs in healthy human SC (11,42). The fully atomistic CHARMM36 force field (43) supplemented by the CHARMM-compatible CER headgroup parameters from Guo et al. (29) was used to describe CER NS, CHOL, and FFA. The CER headgroup parameters have been shown to accurately reproduce the thermotropic phase behavior of bilayers composed of pure CER NS (29), and have been used to study the hydration of CER NS headgroups in solution (44,45). Water was modeled using TIP3P (46).

Methods

Lipid monolayers were first constructed by placing 64 lipids on a rectangular lattice in the *xy* plane with 50 $Å^2$ per lipid. Four initial lateral

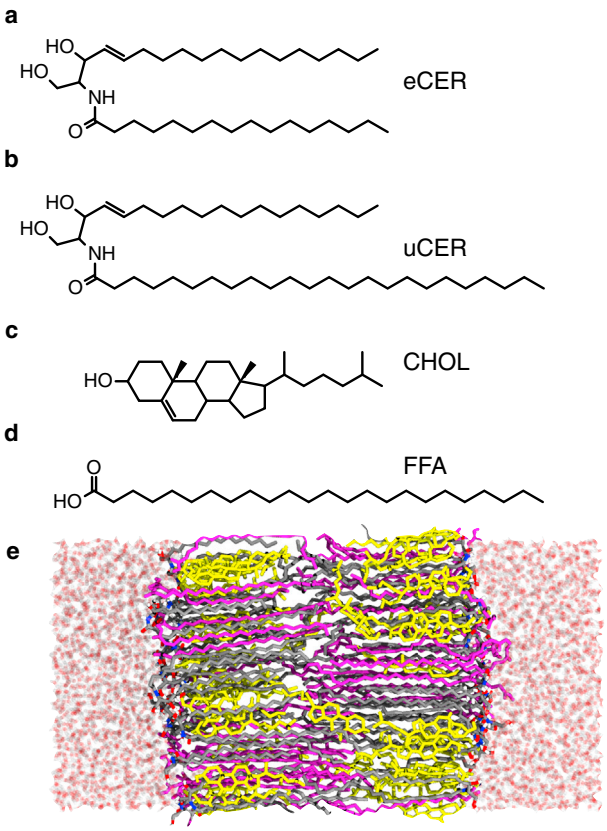

FIGURE 1 Chemical structure of the lipids in this study: (*a*) CER NS C16 (eCER); (*b*) CER NS C24 (uCER); (*c*) cholesterol (CHOL); and (*d*) FFA C24:0 (FFA). (*e*) Snapshot of a typical configuration for the equimolar uCER/CHOL/FFA bilayer. CER is shown in gray, CHOL is shown in yellow, FFA is shown in purple, and water is shown in transparent red (oxygens) and white (hydrogen). To see this figure in color, go online.

distributions of a binary mixture of eCER and CHOL (i.e., different arrangements of lipid species on the lattice) were considered for validating the RWMD approach: completely phase separated, consisting of one 8×4 block of either lipid species (Fig. 2 *a*); a coarse-grained checkerboard, consisting of alternating 4×4 blocks of each lipid species (Fig. 2 *b*); randomly mixed, where both lipid species are randomly dispersed throughout the lattice (Fig. 2 *c*); and a fine-grained checkerboard, consisting of alternating lipid species on the lattice sites (Fig. 2 *d*). To examine the impact of the CER NS FA chain length on structural properties, each of the four lipid compositions studied (pure CER NS, 2:1 CER NS/CHOL, 1:1 CER NS/CHOL, and equimolar CER NS/CHOL/FFA) was divided into five subcompositions, where the CER NS fraction consists of 0, 25, 50, 75, and 100 mol % eCER. Thus, in total, 20 such systems were considered. For these simulations, the effect of the initial lateral distributions of the lipids was not explored, and the different lipid species were initially randomly dispersed throughout the lattice, with the number of each specific lipid dictated by the system composition.

In all cases, each lipid was rotated about its long axis by a random integer multiple of 60°, since a high degree of alignment between lipid backbones has been shown to cause unphysically large tilt angles in the lipid tails of gel-phase bilayers (39). The monolayer was then rotated about the x axis and translated in z such that the ends of the tails in opposing leaflets were in contact, forming a bilayer; it should be noted that in this procedure, each leaflet starts with the same in-plane configuration. Twenty water molecules per lipid were then added to hydrate the outside of the bilayers (2560 total water molecules for 128 total lipids). System sizes ranged from 19,136 to 24,192 atoms.

The systems were relaxed through a series of energy minimization, NVT simulations, and NPT simulations. First, a steepest-descent energy minimization was performed on each initial configuration to reduce the large nonbonded repulsions caused by (inadvertently) overlapping atoms. Next, the systems were simulated for 10 ps in the NVT ensemble at 305 K (i.e., skin temperature), and then for 10 ns in the NPT ensemble at 305 K and 1 atm. Unless otherwise noted, the systems were further simulated using the RWMD algorithm. In the RWMD algorithm, the system temperature is adjusted at small time intervals, such that the system takes a random walk through temperature space. Specifically, the sequence is defined within an interval between T_{min} and T_{max}, with discrete temperatures defined every ΔT. In this work, RWMD was performed for 50 ns, with temperature changes of $\Delta T = 5 \times j (j \in \{-1, 0, 1\}) K$ every 5 ps, $T_{min} = 305$ K, and T_{max} set to 355 K for the first 25 ns and linearly reduced to 305 K over the final 25 ns. A representative plot of temperature versus time during the RWMD equilibration is shown in Fig. S1, where, we note, the sequence is defined such that it samples all temperature states equally. Systems were further simulated at 305 K for at least 150 ns after RWMD. Note that 200 ns of simulation at a fixed temperature range is used for comparison to the results obtained from simulations with RWMD in the RWMD validation section (i.e., for the RWMD validation, the 305 K systems were simulated for 200 ns at 305 K, and the RWMD systems were simulated for 200 ns with $T_{min} = 305$ K and $T_{max} = 355$ K). To avoid modification of the simulation code itself, we note that this random walk was determined separately and the sequence of temperatures provided to the thermostat.

The RWMD approach is designed to mimic key aspects of the Monte Carlo simulated tempering (ST) algorithm (47), used to find minima on a rough free-energy surface by dynamically adjusting the temperature throughout the course of a simulation. The general idea of the ST algorithm is that increasing the system temperature lowers free-energy barriers, allowing different local minima to be explored each time the system returns from an elevated temperature to the (lower) temperature of interest, all while keeping the system at equilibrium, because the acceptance criterion used to accept or reject temperature swaps ensures that the configurations sample the correct equilibrium ensemble (47). The acceptance criterion distinguishes the ST approach from the widely used simulated annealing method, in which a system is driven out of equilibrium by increasing its temperature and simulating for a long time at the elevated temperature, followed by a slow cooling to the temperature of interest. Note that we define a random temperature walk before the simulation, in contrast to the original ST algorithm, which involves attempting a temperature swap after each sweep in a Monte Carlo simulation using the standard Metropolis acceptance/rejection criteria, ultimately yielding a random walk through temperature space.

All simulations were performed in GROMACS 5.1 (48), employing the Nosé-Hoover thermostat (49) with a coupling constant of 1 ps and, for the NPT simulations, a Parrinello-Rahman barostat (50) with a coupling constant of 10 ps. The pressure was controlled semi-isotropically for all NPT simulations, where the box lengths of the bilayer lateral directions were coupled. van der Waals interactions were smoothly switched off between 10 and 12 Å, beyond which they were neglected. Long-range electrostatic interactions were treated via the particle-mesh Ewald algorithm (51) with a real-space cutoff of 12 Å. A time step of 1 fs was used for all simulations. Note that separate thermostats were used for the lipids and the water, although both groups follow the same temperature walk to avoid introducing temperature gradients into the system.

Analysis

System properties were calculated over the final 100 ns of simulation at 305 K. To quantify the structure of the bilayer, various properties were calculated, including the area per lipid (APL), the tilt angle of the lipid tails with respect to the bilayer normal (i.e., the z axis), the area per tail (APT), the nematic order parameter, density profiles of various groups across the bilayer normal, the bilayer thickness, the width of the lipid-water interface, the width of the low-density tail region, and the hydrogen bonding. The

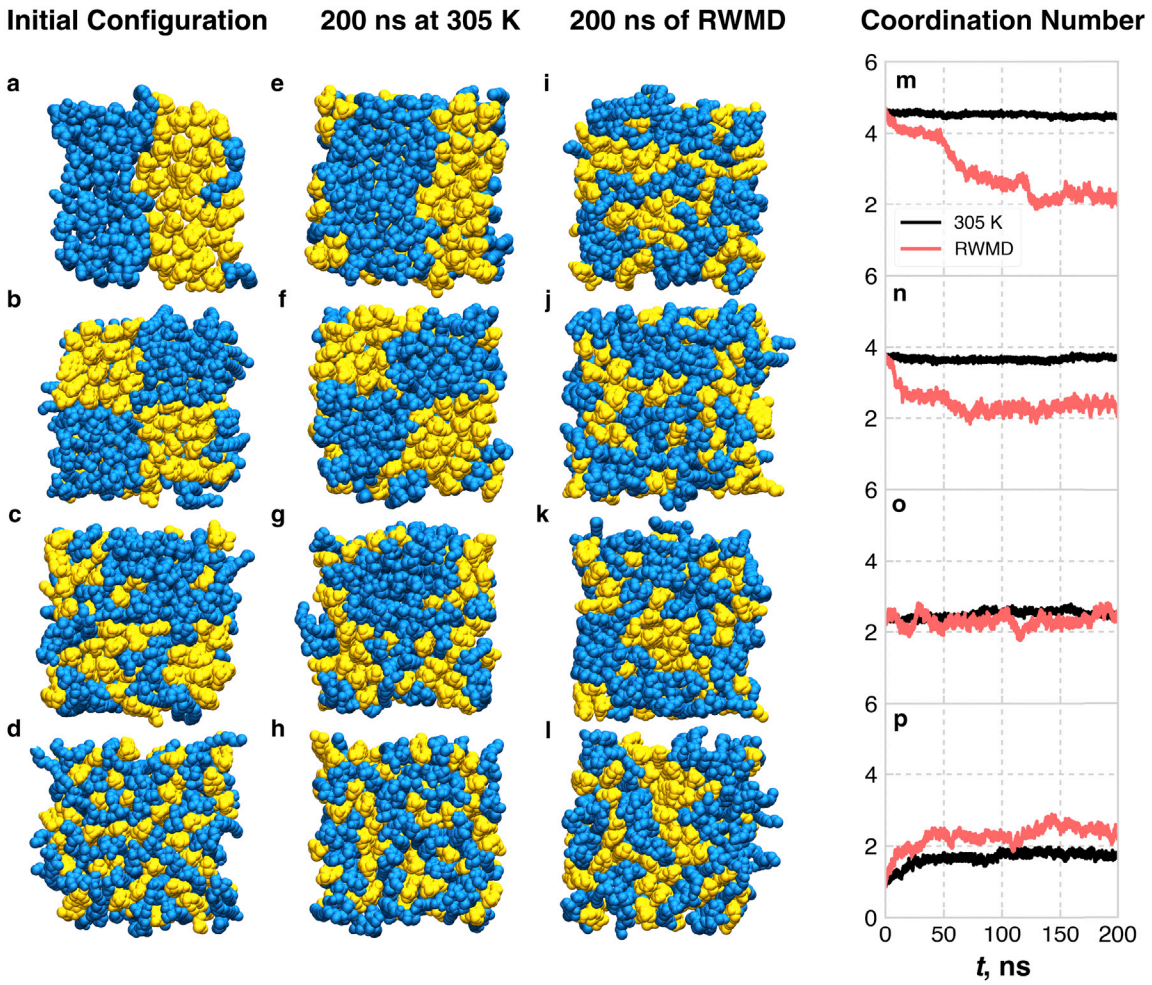

FIGURE 2 System configurations and CHOL-CHOL CN as a function of initial configuration and equilibration procedure for the equimolar mixture of eCER and CHOL. The first column shows the different initial configurations: (*a*) maximum phase separation; (*b*) Coarse-grained checkerboard; (*c*) randomly mixed; and (*d*) Fine-grained checkerboard. The second column shows the systems after 200 ns of MD at 305 K (*e–h*), the third column shows the systems after 200 ns of RWMD (*i–l*), and the fourth column shows the evolution of the CHOL-CHOL CN for each initial configuration (*m–p*). Snapshots are taken along the z axis, i.e., along the bilayer normal direction. eCER is represented as blue spheres and CHOL as yellow spheres. For clarity, water is not shown. To see this figure in color, go online.

coordination numbers (CNs) of different lipid tail pairs in the bilayer plane are used to describe the lateral distributions of lipids; the center of mass of each tail is projected onto the $z = 0$ plane for these calculations. Note that the tails were chosen for the CN calculations, because the lipid tails pack in an ordered hexagonal lattice, in contrast to the relatively more disordered packing of the lipid headgroups. The lipid backbone orientation is used to describe the rotational motion of the lipids about their long axes. A detailed description of each of these calculations is given in the Supporting Material.

RESULTS

RWMD

Before using the RWMD scheme in the rest of this work, the efficacy of the approach is first evaluated for equimolar mixtures of eCER and CHOL. This composition was chosen because eCER and CHOL have similar hydrophobic lengths, which should yield bilayers without a considerable interdigitation region in the middle; prior work has shown that CHOL can reside in this interdigitation region in lipid mixtures with uCER (28). Thus, the lipids (especially CHOL) in this mixture should stay in their canonical bilayer conformation, i.e., with their headgroups at the lipid-water interface and their tails creating a hydrophobic core, therefore allowing evaluation of the ability of RWMD to enhance the in-plane lateral and rotational rearrangements of the lipids.

Fig. 2 shows the initial configuration of each system studied, the final configurations at 200 ns at 305 K, the final configurations after 200 ns of RWMD, and the evolution of the CHOL-CHOL CNs for each equilibration scheme. Note that the CHOL-CHOL CN was chosen because it is the least biased CN (e.g., the FA-SPH CN is skewed, because the FA and SPH tails are part of the same molecule and hence will show a high level of association). Since lipids of the

equimolar eCER-CHOL mixture are expected to mix, the fully separated and coarse-grained checkerboard morphologies (Fig. 2, *a* and *b*) serve as "bad" initial configurations, and the randomly mixed and fine-grained checkerboard systems (Fig. 2, *c* and *d*) serve as naïve, but reasonable, guesses of how to initialize mixed-lipid bilayers. Each initial morphology was equilibrated for 200 ns with two different schemes: standard MD at 305 K, and RWMD with 305 K $< T <$ 355 K. Both visual inspection and the evolution of the CHOL-CHOL CN can be used to compare the in-plane morphologies, and hence equilibration, of the different systems and equilibration procedures. At 305 K, the final morphologies visually resemble the corresponding initial morphologies; this is reflected in the steady-state nature of the CNs at 305 K, which are listed in Table 1. This is especially notable for the fully separated and coarse-grained checkerboard systems, where the large CHOL aggregates make it easy to visually establish that there are only slight changes in the shape of the initial aggregates. These results highlight the frozen nature of these systems at 305 K; only small rearrangements occur in 200 ns if RWMD is not applied. Note that in the fine-grained checkerboard system, small linear aggregates of CHOL form relatively quickly, indicated by the increase in the CN during the first 25 ns, although the system does not evolve much after this initial change.

With RWMD, the final lateral distributions of the lipids are visually distinct from the initial configuration, showing that the lipids were able to reorganize within the bilayer leaflets. For the two most separated systems, the larger CHOL aggregates mostly break up into smaller aggregates (Fig. 2, *a*, *b*, *i*, and *j*), although small CHOL aggregates form in the fine-grained checkerboard system (Fig. 2, *d* and *l*). Importantly, all of the final configurations after RWMD visually resemble each other and have nearly identical CN values, as listed in Table 1, and systems that start close to the final morphology (i.e., the random and fine-grained checkerboard) rapidly converge to their final CN. Since each of these systems started from qualitatively different initial configurations, this result shows that the final configurations are decorrelated from the initial configurations and RWMD can reproducibly form structures with matching properties without strong bias from the starting configuration. We note that this does not necessarily indicate that RWMD has found the true free-energy minimum of the system, but it does strongly suggest that the final configuration is a stable, low-energy configuration, given that multiple independent trajectories converge to the same state.

TABLE 1 CHOL-CHOL CN Over the Final 50 ns of MD Simulation

	Initial Configuration			
Equilibration	Separated	CG Checker	Random Mix	FG Checker
305 K	4.46 ± 0.03	3.72 ± 0.04	2.53 ± 0.08	1.75 ± 0.07
RWMD	2.3 ± 0.1	2.4 ± 0.1	2.4 ± 0.2	2.5 ± 0.1

"Separated" refers to the initial configuration shown in Fig. 2 *a*, "CG Checker" to that in Fig. 2 *b*, "Random Mix" to that in Fig. 2 *c*, and "FG Checker" to that in Fig. 2 *d*. The uncertainties here, and in all subsequent tables and figures, are given as the SE of the measured property.

Analysis of the rotational motion of the eCER molecules also suggests that the systems equilibrated with RWMD are more decorrelated from their initial configurations than those equilibrated at 305 K. Fig. 3 shows the autocorrelation function of the lipid backbone angle in the bilayer plane for the different initial configurations and equilibration methods. The lipid backbone orientations become completely uncorrelated from the initial orientations by 25 ns of RWMD, whereas slower relaxation is observed for the systems simulated at 305 K. Interestingly, the phase-separated system shows the slowest relaxation of the eCER backbone orientations, likely because the large, dense eCER domain has a larger energy barrier for lipid rotation due to lipid-lipid hydrogen bonding. Since the systems that were equilibrated at 305 K all converge to different morphologies and the lipid backbone orientations are correlated to the initial orientations, at least three of the four systems must be metastable configurations. Often in bilayer simulations, a specific property, such as the area per lipid (APL), is monitored over time, and equilibrium is assumed when that property reaches a steady state. This practice, however, may lead to spurious assumptions of equilibrium, since other features of the bilayer structure may not exist in their preferred state, but this cannot be easily verified since the preferred state is not always known a priori. For example, the APLs of the systems equilibrated at 305 K are compared to the APLs of the systems equilibrated with RWMD (after running at 305 K for a more direct comparison) in Table 2, from which it is apparent that the systems equilibrated at 305 K show a larger spread in the APLs than the systems equilibrated with RWMD. The two systems with the highest level of CHOL aggregation have similar APLs, whereas the other two systems have lower APLs that are similar to each other. Due to the different morphologies and packing densities of the lipids in these systems, they likely have different properties, e.g., permeability, which is related to the in-plane density of the lipids (52). In contrast, all of the systems equilibrated with RWMD have APLs consistent within the standard deviation, further illustrating their reproducibility, and hence confidence gained, when equilibrating with RWMD.

This lack of mobility and difficulty in proper equilibration is a recognized problem when simulating CER-based bilayers, with many studies running the systems at elevated temperatures in an attempt to overcome mobility issues (25–28,30,31,34,35). Here, we also compare to equilibration and production runs at 340 K, as several MD studies of SC lipids have used this temperature (25–28). Fig. 4 shows the evolution of the CN for the fully separated system (Fig. 2 *a*) simulated for 600 ns at 305 K and 340 K, and with

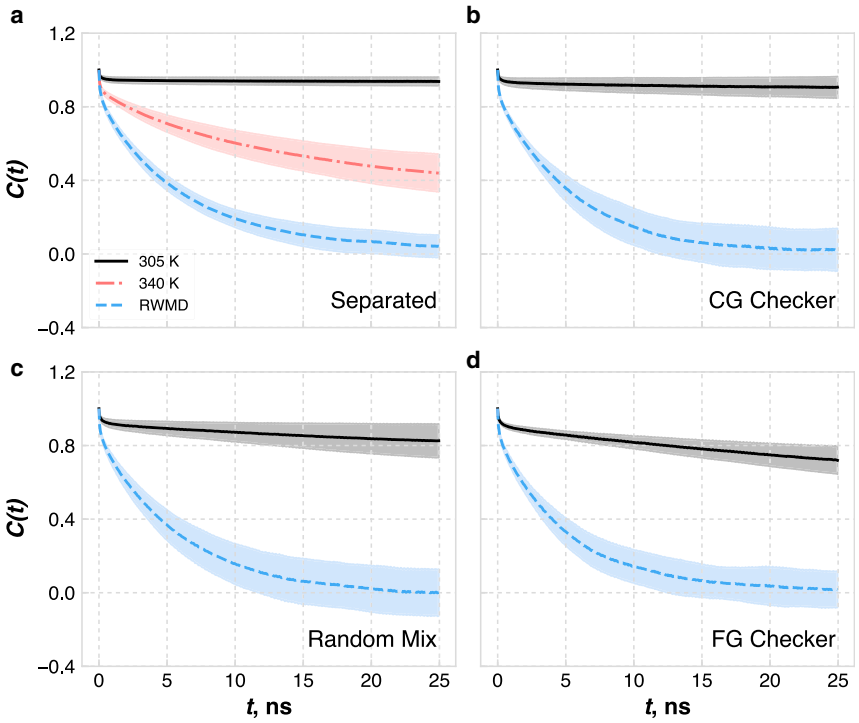

FIGURE 3 Autocorrelation function, $C(t)$, of the eCER backbone orientations during simulations at 305 K and with RWMD from different initial configurations. "Separated" (*a*) refers to Fig. 2 *a*, "CG Checker" (*b*) to Fig. 2 *b*, "Random Mix" (*c*) to Fig. 2 *c*, and "FG Checker" (*d*) to Fig. 2 *d*. The shaded area shown is the standard deviation over the rotational autocorrelation function of all eCER molecules in the bilayer. To see this figure in color, go online.

RWMD. As expected, the system at 305 K is still frozen in simulations in excess of 0.5 μs, whereas the system simulated with RWMD reaches its steady-state CN number after ~110 ns. Perhaps unsurprisingly, the system simulated at 340 K shows behavior somewhere in between that of the other systems; although lateral reorganization does occur, the CN reaches a steady-state value after ~520 ns, which we note is significantly longer than the simulation times typically studied. Note that this system also reaches a pseudo-steady-state CN between 80 and 150 ns; with many studies performed on simulations run for 100 ns or less, this metastable state could be erroneously mistaken for equilibrium, if one were relying on the CN to determine convergence. At 600 ns, the rotational relaxation of the lipids for this system at 340 K is higher than at 305 K, but still lower than for RWMD (Fig. 3 *a*). Although the fully phase-separated system is likely a poorly chosen starting configuration given some level of prior knowledge of this particular system, we emphasize that the actual morphology is typically not known a priori. Thus, these results indicate that RWMD is more efficient than simply running at a high temperature to equilibrate multicomponent, gel-phase lipid bilayers and can provide increased confidence in the reproducibility of the results, particularly for systems in which the lateral organization is unknown and expected to play an important role in properties of interest.

TABLE 2 APL of Systems as a Function of Initial Configuration and Equilibration Methodology

	Initial Configuration			
Equilibration	Separated	CG Checker	Random Mix	FG Checker
305 K	38.8 ± 0.4	38.8 ± 0.4	39.4 ± 0.2	39.6 ± 0.2
RWMD	39.6 ± 0.5	39.7 ± 0.4	39.5 ± 0.4	39.4 ± 0.3

APL values are given in Ängstroms squared (Ä^2). The systems equilibrated with RWMD were simulated at 305 K for 50 ns for a more direct comparison with the other systems. "Separated" refers to Fig. 2 *a*, "CG Checker" to Fig. 2 *b*, "Random Mix" to Fig. 2 *c*, and "FG Checker" to Fig. 2 *d*.

Dependence of structural properties on bilayer composition

The effect of the composition of CER-based lipid bilayers on structural properties is now examined. It should be noted

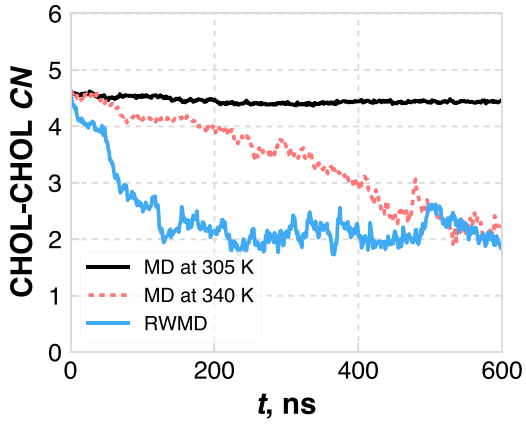

FIGURE 4 Evolution of the CHOL-CHOL CN for the fully phase-separated systems equilibrated with three different methodologies as a function of time (t). To see this figure in color, go online.

that all systems start from a randomly dispersed morphology, given that this arrangement relaxed the fastest and appears to be reasonably representative of the morphology for this family of systems, as discussed in the previous section; these systems were also relaxed using RWMD, as described in Materials and Methods.

General structural properties

All systems exist in dense, highly ordered gel phases, as indicated by high nematic order parameters ranging from 0.95 to 0.99, shown in Fig. S4 and Table S1. The addition of CHOL decreases the nematic order, consistent with Das et al. (26), but the magnitude of this decrease is quite small (e.g., ranging from 0.988 for pure uCER to 0.954 for 1:1 CER/CHOL with 3:1 eCER/uCER) and the lipids are still highly ordered from visual inspection (Fig. 1 *e*), indicating no phase change upon addition of CHOL for these compositions.

The tilt angle shows a weak dependence on composition, as shown in Fig. 5 *a*. The tilt angle depends significantly on the CER FA tail length for the pure CER systems, where a strong increase is seen with increasing eCER for systems with 50% or more eCER. This trend is a result of the balance between headgroup and tail interactions: steric repulsions between lipid headgroups dictate the APL, whereas van der Waals attractions between the lipid tails cause them to tilt to optimize their spacing (53). For the CER bilayers that are predominantly uCER, the tail length asymmetry gives rise to a wide low-density tail region in the center of the bilayer (discussed below), which increases the effective optimal tail packing, leading to a lower tilt angle. The addition of CHOL and FFA causes the tails to tilt less and show almost no change as a function of increasing eCER, likely because CHOL has a bulky ring structure with a small headgroup and therefore acts as a spacer between the lipid tails, buffering the head-tail effects seen in the pure systems. Hence, there is a smaller mismatch between the packing densities of the headgroups and tails, leading to a smaller tilt. Notably, the 1:1 CER/CHOL and ternary mixtures have very similar tilt angles, which we attribute to the fact that these systems have a similar fraction of alkyl tails.

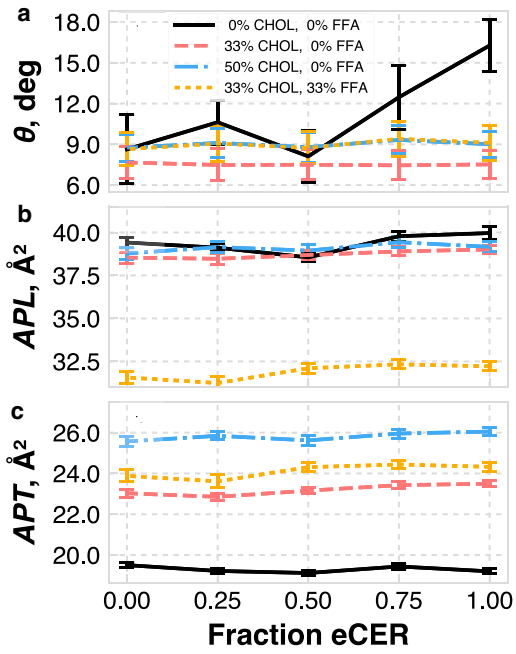

FIGURE 5 (*a*) Average tilt angle (θ) of the lipid tails with respect to the bilayer normal, (*b*) APL, and (*c*) APT as a function of eCER composition. Note that the abscissa is the fraction of CER NS that is eCER, not the total eCER fraction in the system. To see this figure in color, go online.

The APL and APT trends as a function of the fraction of eCER are shown in Fig. 5, *b* and *c*. Although the APL describes the density of lipids in the bilayer plane, irrespective of the number of tails that each lipid has, the APT describes the tail packing density in the plane of the lipid tails (i.e., APT accounts for both the number of tails and the tilt angle). All CER NS and CER NS/CHOL systems have similar APLs, between 38 and 40 $Å^2$, as expected, since CER and CHOL have similar cross-sectional areas (54). There is only a slight, nonmonotonic dependence of the APL on CER FA tail length. This trend is expected, since the headgroups dictate the APL and these systems have the same headgroups for a given composition. Systems containing FFAs have smaller APLs, since FFA contains a single alkyl chain. The APT increases with CHOL content, as CHOL and CER NS have similar cross-sectional areas, but CHOL is treated as a single tail. The ternary systems have APTs more similar to the 2:1 CER NS/CHOL systems, which is reasonable considering that they have the same ratio of CHOL to alkyl chains. The mixed lipid systems all show a slightly increasing APT with increasing eCER fraction. Interestingly, there appears to be some level of APT nonadditivity in these systems. For example, consider the APLs and APTs of the 1:1 CER NS/CHOL systems. Since they have APLs similar to those of the pure CER NS systems, but 3/4 the number of tails, ideal mixing would yield APL values that are 4/3 that of the pure CER NS values. However, the actual values are lower, suggesting a relative attraction between CHOL and the saturated tails of CER NS, similar to what was observed for dimyristoylphosphocholine (DMPC, a phospholipid with saturated tails), but not for dioleoylphosphocholine (DOPC, a phospholipid with unsaturated tails) (55). Although perhaps expected, based on chain saturation, this behavior is nontrivial for CER systems, since the CER NS headgroups are much smaller than PC headgroups and CHOL presumably has less empty space to occupy.

Density profiles

The bilayer thickness, calculated from the water density profiles, is a function of both overall lipid composition and CER FA tail length (Fig. S5 and Table S2). The bilayer

thickness decreases with increasing eCER and CHOL content, as one would expect, since these lipids have shorter tail lengths than uCER or FFA. However, the tail-length asymmetry leads to a richer behavior, which can be observed via examination of the lipid density profiles, as shown for each system in Fig. 6.

The pure CER bilayers exhibit mass density profiles that contain the expected features of a lipid bilayer. Near the lipid-water interface, the profiles contain a peak (Fig. 6 *a*), which represents the heavy atoms in the CER headgroups. Just inside the headgroup region, there is a high-density tail region where the tails are densely packed and highly ordered (see discussion of nematic order above), consistent with prior work (37). In the center of the bilayer is a low-density tail region where the lipid tails are less densely packed and less ordered. This region exists primarily due to the asymmetry in the lengths of the tails in the systems and is composed of the terminal part of the uCER tail and FFA tails, as shown in Fig. S6. In the systems with less asymmetry (i.e., high eCER and CHOL concentrations), the profile is more V-shaped in the middle, since there is little interdigitation between tails in opposing leaflets. Comparing the high- and low-density tail regions for the different bilayers, the width of the high-density tail region is found to be nearly constant across all compositions, whereas the width of the low-density tail region varies with eCER and CHOL content. Fig. 7 shows the total bilayer thickness as a function of the thickness of this low-density tail region in the center of the bilayer. Clearly, the thickness of the low-density tail region dictates the total bilayer thickness for a given composition. The width of the high-density tail region is determined by the smallest hydrophobic length in the system, where the tails must pack densely to fit into the area dictated by the headgroups. For the lipids in this study, this is ~16 carbons, or the length of the sphingosine chain that is not part of the CER NS headgroup, which is also similar to the length of a CHOL molecule (56).

The presence of CHOL and FFA has two main effects on the density profiles. First, the smaller headgroups of CHOL and FFA lead to smaller peaks in the headgroup region, compared to a pure CER NS bilayer; these peaks are dramatically reduced going from pure CER to 2:1 CER NS/CHOL and are mostly absent in the 1:1 CER NS/CHOL and ternary systems. Second, the width of the low-density tail region increases with the addition of CHOL and FFA, as shown in Figs. 6 and 7. Additionally, the low-density tail regions tend to have more features in the mixed-lipid systems, e.g., shoulders representing intermediate densities due to the different tail lengths. Peaks also appear in the middle of the density profiles for the mixed systems, due both to the long FA chain of uCER (and FFA for the three-component system) and the presence of CHOL that has migrated from the ordered bilayer region into the low-density tail region (28). In the eCER/CHOL systems, the lack of significant interdigitation means this peak is absent; however, all systems containing FFA demonstrate a peak in the middle of the density profile because of the long tail of FFA.

Fig. 8 shows the density profiles for the ternary system with 1:1 eCER/uCER, along the bilayer normal direction,

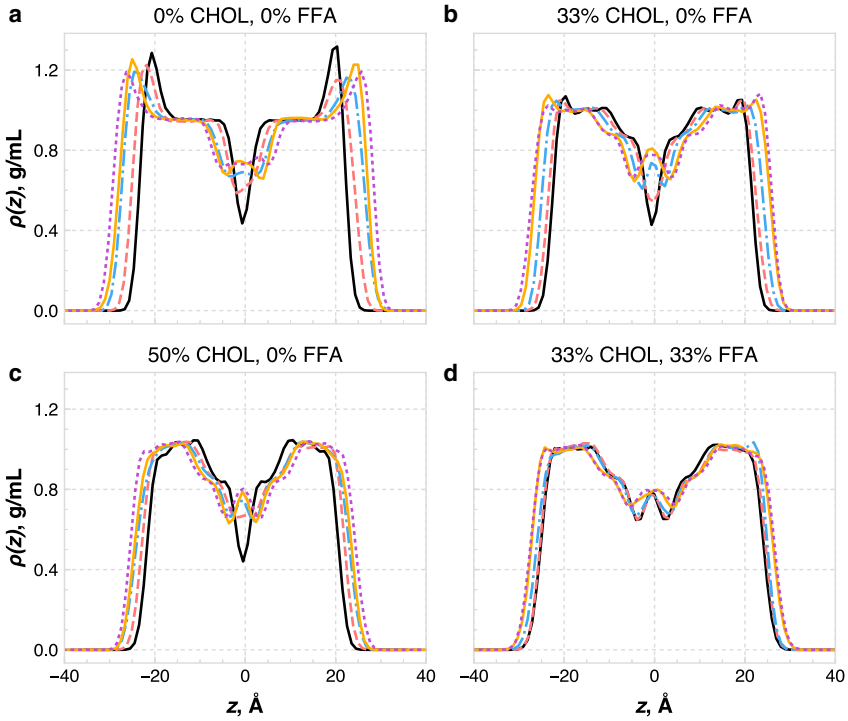

FIGURE 6 Total lipid mass density profiles across the bilayer for all systems considered: (*a*) pure CER NS, (*b*) 2:1 CER NS/CHOL, (*c*) 1:1 CER NS/CHOL, and (*d*) equimolar CER NS/CHOL/FFA. The profiles for the five subcompositions are shown for all compositions and are labeled as follows: solid black line, 100 mol % eCER; dashed red line, 75 mol % eCER; dot-dashed blue line, 50 mol % eCER; solid orange line, 25 mol % eCER; dotted purple line, 0 mol % eCER. Note that these percentages denote the fraction of CER NS that is eCER, not the total fraction of eCER in the system. To see this figure in color, go online.

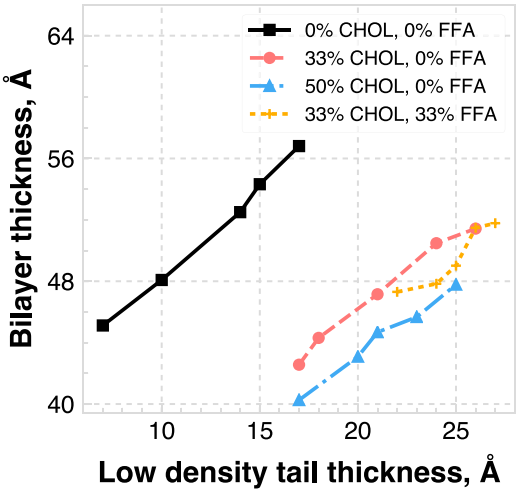

FIGURE 7 Total bilayer thickness as a function of the thickness of the low-density tail region, with the different points on each line denoting the different eCER fractions; the smallest values indicate 100 mol % eCER, and the largest 0 mol % eCER. To see this figure in color, go online.

broken down by the contribution of specific lipid components. The CHOL headgroup sits ~3 Å deeper in the bilayer with respect to the CER headgroups, which is consistent with prior simulation and experimental studies (23,26,31). There is also a small subpopulation of CHOL lying flat in the middle of the bilayer, illustrated by the peak in the middle of the CHOL ring density profile, which is consistent with the work of Das et al. (28) Additionally, the FFA headgroups tend to sit slightly farther into the water than the CER headgroups.

The interfacial width, which can indicate the hydrophobicity of the surface (e.g., a larger interfacial width would indicate a more hydrophilic surface), is defined as the width of the region over which the water density drops from the bulk value to 1/*e* of the bulk value. The bilayers in this

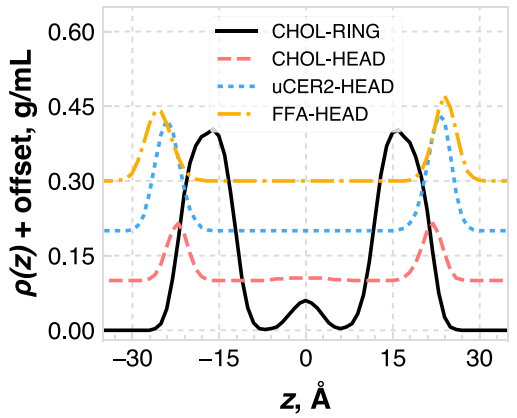

FIGURE 8 Mass density profiles of various groups in the ternary bilayer with a 1:1 eCER/uCER composition. Note that the profiles for different groups are shifted vertically for clarity. Each curve is offset by 0.1 g/mL for each subsequent data set in the legend. To see this figure in color, go online.

work appear hydrophobic, having interfacial thicknesses between 3.5 and 6 Å, as compared to phospholipid bilayers, which are generally >10 Å (57). There is little dependence on the bilayer composition or CER FA tail length, as shown in Fig. S7 and Table S3. Thus, we conclude that although the lamellar organization near the middle of the bilayer depends on the lipid composition, the apparent hydrophobicity of the lipid-water interface does not.

Hydrogen bonding

The total numbers of lipid-lipid hydrogen bonds in each system are listed in Table 3. The lipid-lipid hydrogen bonding is a function of the total CER content, with a reduction in CERs resulting in fewer lipid-lipid hydrogen bonds, because CHOL and FFA molecules have fewer hydrogen-bonding sites. The lipid-lipid hydrogen bonding is also independent of the eCER fraction, which can be expected, since eCER and uCER have identical headgroups and their relative position at the interface is essentially unchanged as a function of the eCER fraction.

The hydrogen bonding between specific pairs of lipids for the ternary mixture with 1:1 eCER/uCER is listed in Table S4. Negligible CHOL-CHOL hydrogen bonding is observed, which can be rationalized by the fact that CHOL only has one hydrogen-bond donor and acceptor, and two neighboring CHOL molecules would have to adopt a strained configuration to form a hydrogen bond. There are also very few CHOL-FFA hydrogen bonds, likely a result of CHOL sitting deeper in the bilayer. An appreciable number of CER-CHOL hydrogen bonds are seen, with slightly more eCER-CHOL (4.3) than uCER-CHOL (3.7) hydrogen bonds. Interestingly, the level of CER-CHOL hydrogen bonding is similar in the 2:1 and 1:1 CER/CHOL systems with, for example, 11.4 and 11.1 total CER-CHOL hydrogen bonds for the 2:1 and 1:1 CER/CHOL systems with 50 mol % eCER (Tables S5 and S6); this trend may suggest that CER-CHOL hydrogen bonding is saturated at or below 33 mol % CHOL. Additionally, when CER is replaced by CHOL (i.e., comparing the pure CER NS and the 2:1 CER NS/CHOL or 1:1 CER NS/CHOL systems), there are fewer hydrogen bonds relative to the total number of hydrogen-bonding sites in the system, indicating that

TABLE 3 Total Number of Lipid-Lipid and Lipid-Water Hydrogen Bonds for Each System Studied

		Fraction eCER				
	Composition	0	0.25	0.50	0.75	1.0
Lipid-Lipid	Pure CER NS	63	62	61	63	63
	2:1 CER NS/CHOL	40	37	38	39	38
	1:1 CER NS/CHOL	28	26	28	28	27
	Ternary	19	19	19	19	19
Lipid-Water	Pure CER NS	173	168	173	176	171
	2:1 CER NS/CHOL	173	169	173	175	176
	1:1 CER NS/CHOL	168	170	164	167	173
	Ternary	154	152	158	158	155

CER-CER hydrogen bonds are preferred over CER-CHOL hydrogen bonds. There are comparatively fewer CER-CHOL hydrogen bonds in the ternary systems, since FFA is present and is competing with CHOL to form hydrogen bonds with the CER. There are surprisingly few FFA-FFA hydrogen bonds, given that FFA prefers to be near other FFA molecules (discussed below); however, FFA sits deeper in the water and thus forms more hydrogen bonds with water.

The amount of lipid-water hydrogen bonding in each system is also listed in Table 3. Despite the relatively hydrophobic lipid-water interface, there are significantly more lipid-water hydrogen bonds than lipid-lipid hydrogen bonds. As with the lipid-lipid hydrogen bonds, lipid-water hydrogen bonding is independent of the CER FA tail length. Interestingly, the pure CER and 2:1 CER/CHOL systems have similar amounts of lipid-water hydrogen bonds, despite the fact that CHOL has significantly fewer hydrogen-bonding sites than CER, although the 1:1 CER/CHOL and ternary systems have comparably fewer lipid-water hydrogen bonds, since these systems have less CER (and hence fewer hydrogen-bonding sites) than systems with the other two compositions. This trend in lipid-water hydrogen bonding is perhaps explained by the "spacer" effect of CHOL, discussed above with respect to the tilt angles. Although less CER results in fewer available hydrogen-bonding sites, the spacing effect of CHOL allows the water to more thoroughly hydrate the CER headgroups and hence results in more lipid-water hydrogen bonds per hydrogen bonding site.

In-plane morphology

For a general view of the in-plane morphology of each system, we examine CNs between specific lipid tails in the bilayer plane. The CHOL-CHOL CNs depend on the amount of CHOL and available neighbors in a given system, and not on the CER FA tail length, as detailed in Fig. S8 and Table S7. This result suggests a random distribution of CHOL throughout the bilayer leaflets. For example, there are equal numbers of three different types of tails in the 1:1 CER/CHOL systems (i.e., CER-FA, CER-SPH, and CHOL). Random mixing would give the observed CHOL-CHOL CN of 2. Applying this logic to the 2:1 CER/CHOL and ternary systems, random mixing would imply CHOL-CHOL CNs of 1.2 and 1.5 for each composition, respectively, which is observed. In contrast to CHOL, FFA shows a preference for specific neighbors and thus has a less random distribution throughout the bilayer leaflets. In the uCER/CHOL/FFA system, the FFA-CER_{FA} and FFA-CER_{SPH} CNs are 1.39 ± 0.08 and 1.20 ± 0.07, respectively (where CER_{FA} and CER_{SPH} represent the FA and sphingosine tails of CER, respectively). This result suggests that FFA has a preference for the FA chain of CER compared to the SPH chain. Additionally, a significant preference for FFA to be near FFA is observed, with an FFA-FFA CN of 2.3 ± 0.1, compared to 1.39 ± 0.08 for FFA-CER_{FA}, the second highest. This has also been observed experimentally, with FFA-enriched domains forming with the tails tightly packed on an orthorhombic lattice (19). However, unlike experimental results on similar systems (41), we do not see any chain-length-dependent behavior with regard to the mixing of CER and FFA. We note, though, that comparable experimental systems consider multilamellar structures, whereas we consider a single hydrated bilayer, which could account for the differences observed. We also note that the systems studied in this work are several orders of magnitude smaller than comparable experimental systems (nanometers versus micrometers), and that an in-depth study of lateral distributions of lipids is beyond the scope of this work.

DISCUSSION

Relevance to experimental models of the short periodicity phase

The localization of different groups within an experimental model of the short-periodicity phase (SPP) of the SC has been studied with neutron diffraction (22,23). These experimental systems resemble the systems studied here, with a few differences. First, we only consider CER NS, whereas experimental systems tend to include a mixture of CERs with different headgroups, although uCER typically accounts for the majority (∼60%) of the CERs (11,23). Second, we also only consider FFA C24, whereas experimental systems often include FFAs with a distribution of tail lengths. We note, however, that recent work has shown that CER headgroup chemistry does not play a strong role in the lamellar organization of SPP models, and that systems with a distribution of FFA tail lengths had the same lamellar organization as a similar system with only FFA C24 (11). Perhaps the biggest difference between experimental systems and the systems studied here is that we consider a single bilayer, which is the typical approach to studying these systems with molecular simulation. Experimental systems usually contain membranes with numerous diffraction orders detected, indicating multilayer structures. Nonetheless, we can directly compare neutron scattering-length density (NSLD) profiles from simulation and experiment. Additionally, we can compare the localization of specific groups based on mass density profiles from simulation and those reconstructed from selective deuteration of specific groups from experiment.

In Fig. 9, we compare the total NSLD profiles from experiment (22,23) and simulation. The most obvious features of each are the large peaks at ±27 Å (experiment) and ±25 Å (simulation). Given the experimental resolution of ∼5.4 Å, the locations of these peaks are in good agreement. It is worth noting that the NSLD profiles calculated from

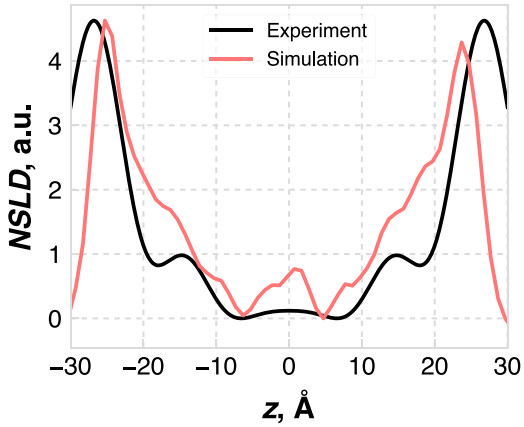

FIGURE 9 NSLD profiles, reconstructed from experiment (22) and calculated from simulation. Note that the profiles were shifted such that the minimum lies at 0, and the simulation curve was scaled to have the same height as the experimental curve. To see this figure in color, go online.

simulation were averaged over multiple subtrajectories from the simulation, and the calculated uncertainty was smaller than the line thickness; this small error is likely due to the fact that the simulation samples tens of Ångstroms over tens of nanoseconds, so small variability in density profiles should be expected. Both simulation and experiment show valleys in the NSLD at ∼7 Å, which we note aligns with the dips in the low-tail-density region from Fig. 6 *d*. Additionally, subtle shoulders in the NSLDs are present at ±15 Å in both simulation and experiment, which aligns with the edges of the low-tail-density region shown in Fig. 6 *d*.

Focusing next on the localization of specific groups within the bilayer, we compare the mass density profiles from simulation with the difference between the protonated and deuterated NSLDs from experiment, shown in Fig. S9. In this manner, we can compare the localization of specific groups between simulation and experiment. Comparing the location of the FA tail of uCER that was measured in Groen et al. (22), we find good agreement, with a single broad peak spanning ±7.5 Å (Fig. S9 *a*), corresponding to the region where the uCER FA tails from opposing leaflets interdigitate. The CHOL tails are localized at ±2 Å in both simulation and experiment (Fig. S9 *b*) (23). The CHOL headgroups show some deviation between experiment and simulation, localized at ±23 and ±21 Å, respectively (Fig. S9 *c*). This discrepancy, however, is again within the experimental resolution of 5.4 Å (23). Despite the fact that we are studying single bilayers, the locations of specific groups within the bilayer agree very well with experimental data on systems with similar compositions. Therefore, we can conclude that the model systems accurately approximate the model SPP systems from experiment, and conclusions from this work also likely apply to model SPP systems, and also to the SPP in the SC.

Effects on barrier properties of SC

In this work, the lipid composition and CER FA tail length were found to have the largest impact on lamellar organization, with the bilayer thickness and shape of the density profile in the low-density tail region most affected. If we consider how these changes would affect the barrier properties (i.e., the permeability) of these bilayers, we can provide some insight into the observed experimental behavior. The permeability of a membrane is a product of the solute diffusion and partitioning, where the partitioning has an exponential dependence on the free energy of solvation. Due to this exponential dependence, small changes in local packing (i.e., depth-dependent density), can have a dominant impact on the bilayer permeability. Since the lipid mass density profiles are not constant across the bilayers, the resistance experienced by a permeant molecule would vary with bilayer depth. Moreover, since the low-density tail regions are qualitatively different for bilayers with different compositions, these depth-dependent partition coefficients would also change, albeit nontrivially. Thus, if one was interested in comparing the permeability of these different systems, a simple homogeneous solubility-diffusion model would not suffice. This indeed is not unrecognized in the field, as the few simulation studies of SC lipid permeability in the literature to date have used an inhomogeneous solubility-diffusion model (30,52).

Although the structure of the lipids at the lipid-water interface changes with composition, it does not change with CER FA tail length. This is illustrated by the fact that the thickness of the interfacial region and lipid density profiles near the headgroups are unchanged with the CER FA tail length for a given composition (Fig. 6; Fig. S7). Additionally, both the total number of lipid-water and lipid-lipid hydrogen bonds is constant for a given composition. Thus, we expect any changes in the barrier properties of model SC membranes with CER FA tail length to be a result of changes in the structure of the bilayers in the hydrophobic core, and that changes in the headgroup region would play only a small role. This observation is consistent with the permeability measurements reported by Uchiyama et al. (11), which show that the permeability of ethyl-*p*-aminobenzoic acid through membranes composed of synthetic mixtures of CER, CHOL, and FFA is independent of the CER composition, but strongly dependent on the FFA tail-length dispersity.

CONCLUSIONS

We have studied via MD simulations the structure of lipid bilayers relevant to the SC layer of the skin, as well as proposed and validated a thorough relaxation protocol for such systems. We first illustrated several difficulties in simulating SC lipid mixtures and multicomponent gel-phase bilayers in general, e.g., that systems tend to be frozen at physiological

temperatures with only small lateral rearrangements possible. Since the most realistic morphologies are not generally known a priori, systems must be allowed to find the most realistic morphology. This task is shown to be computationally impractical at physiological temperatures and inefficient at commonly used elevated temperatures, as well as likely to lead to metastable states being confused for equilibrium states. The proposed RWMD methodology, based on ST, was shown to be an efficient and reproducible method for minimizing the influence of an assumed initial membrane configuration for multicomponent gel-phase bilayers. We therefore expect this method to be especially useful as simulations incorporate more complex lipid mixtures. Using the RWMD protocol, we examined a series of SC lipid bilayers with varying lipid compositions and CER FA tail length. We showed that the lamellar organization is most affected by the lipid composition and CER FA tail length. Subtle changes to the lateral organization of the lipid tails as a function of the CER FA tail length were also seen. Additionally, since it was observed that the behavior at the lipid-water interface does not change with the CER FA tail length, we speculate that any tail-length-dependent changes in barrier function are a result of changes in the lipid tail region and not the headgroup region.

SUPPORTING MATERIAL

Nine figures and seven tables are available at http://www.biophysj.org/biophysj/supplemental/S0006-3495(17)31154-2.

AUTHOR CONTRIBUTIONS

C.M., C.R.I., and A.L.B. designed the research. T.C.M. and C.R.I. performed the research. T.C.M. and R.H. contributed the analytic tools. All authors analyzed data and wrote the article.

ACKNOWLEDGMENTS

This work was supported by grant number R01 AR057886-01 from the National Institute of Arthritis and Musculoskeletal and Skin Diseases and National Science Foundation grant number CBET-1028374. This work was conducted in part using computational resources provided by the National Energy Research Scientific Computing Center, supported by the Office of Science of the Department of Energy under contract number DE-AC02-05CH11231 and the Advanced Computing Center for Research and Education at Vanderbilt University.

REFERENCES

1. Madison, K. C. 2003. Barrier function of the skin: "la raison d'être" of the epidermis. *J. Invest. Dermatol.* 121:231–241.
2. Weerheim, A., and M. Ponec. 2001. Determination of stratum corneum lipid profile by tape stripping in combination with high-performance thin-layer chromatography. *Arch. Dermatol. Res.* 293:191–199.
3. Janssens, M., J. van Smeden, …, J. A. Bouwstra. 2012. Increase in short-chain ceramides correlates with an altered lipid organization and decreased barrier function in atopic eczema patients. *J. Lipid Res.* 53:2755–2766.
4. Lavrijsen, A. P. M., J. A. Bouwstra, …, M. Ponec. 1995. Reduced skin barrier function parallels abnormal stratum corneum lipid organization in patients with lamellar ichthyosis. *J. Invest. Dermatol.* 105:619–624.
5. Pilgram, G. S. K., D. C. Vissers, …, H. K. Koerten. 2001. Aberrant lipid organization in stratum corneum of patients with atopic dermatitis and lamellar ichthyosis. *J. Invest. Dermatol.* 117:710–717.
6. van Smeden, J., M. Janssens, …, J. A. Bouwstra. 2014. Intercellular skin barrier lipid composition and organization in Netherton syndrome patients. *J. Invest. Dermatol.* 134:1238–1245.
7. Ishikawa, J., H. Narita, …, A. Hatamochi. 2010. Changes in the ceramide profile of atopic dermatitis patients. *J. Invest. Dermatol.* 130:2511–2514.
8. Joo, K.-M., J.-H. Hwang, …, K.-M. Lim. 2015. Relationship of ceramide-, and free fatty acid-cholesterol ratios in the stratum corneum with skin barrier function of normal, atopic dermatitis lesional and non-lesional skins. *J. Dermatol. Sci.* 77:71–74.
9. Rabionet, M., K. Gorgas, and R. Sandhoff. 2014. Ceramide synthesis in the epidermis. *Biochim. Biophys. Acta.* 1841:422–434.
10. de Jager, M., W. Groenink, …, J. Bouwstra. 2006. A novel in vitro percutaneous penetration model: evaluation of barrier properties with p-aminobenzoic acid and two of its derivatives. *Pharm. Res.* 23:951–960.
11. Uchiyama, M., M. Oguri, …, J. A. Bouwstra. 2016. Free fatty acids chain length distribution affects the permeability of skin lipid model membranes. *Biochim. Biophys. Acta.* 1858:2050–2059.
12. Garidel, P., B. Fölting, …, A. Kerth. 2010. The microstructure of the stratum corneum lipid barrier: mid-infrared spectroscopic studies of hydrated ceramide:palmitic acid:cholesterol model systems. *Biophys. Chem.* 150:144–156.
13. Lafleur, M. 1998. Phase behaviour of model stratum corneum lipid mixtures: an infrared spectroscopy investigation. *Can. J. Chem.* 76:1501–1511.
14. Mojumdar, E. H., G. S. Gooris, and J. A. Bouwstra. 2015. Phase behavior of skin lipid mixtures: the effect of cholesterol on lipid organization. *Soft Matter.* 11:4326–4336.
15. Mojumdar, E. H., G. S. Gooris, …, J. A. Bouwstra. 2016. Stratum corneum lipid matrix: location of acyl ceramide and cholesterol in the unit cell of the long periodicity phase. *Biochim. Biophys. Acta.* 1858:1926–1934.
16. Moore, D. J., M. E. Rerek, and R. Mendelsohn. 1999. Role of ceramides 2 and 5 in the structure of the stratum corneum lipid barrier. *Int. J. Cosmet. Sci.* 21:353–368.
17. Mueller, J., A. Schroeter, …, R. H. H. Neubert. 2016. Preparation of a new oligolamellar stratum corneum lipid model. *Langmuir.* 32:4673–4680.
18. Rowat, A. C., N. Kitson, and J. L. Thewalt. 2006. Interactions of oleic acid and model stratum corneum membranes as seen by 2H NMR. *Int. J. Pharm.* 307:225–231.
19. Školová, B., B. Janůšová, …, K. Vávrová. 2013. Ceramides in the skin lipid membranes: length matters. *Langmuir.* 29:15624–15633.
20. Školová, B., B. Janůšová, and K. Vávrová. 2016. Ceramides with a pentadecasphingosine chain and short acyls have strong permeabilization effects on skin and model lipid membranes. *Biochim. Biophys. Acta.* 1858:220–232.
21. Velkova, V., and M. Lafleur. 2002. Influence of the lipid composition on the organization of skin lipid model mixtures: an infrared spectroscopy investigation. *Chem. Phys. Lipids.* 117:63–74.
22. Groen, D., G. S. Gooris, …, J. A. Bouwstra. 2011. Disposition of ceramide in model lipid membranes determined by neutron diffraction. *Biophys. J.* 100:1481–1489.
23. Mojumdar, E. H., D. Groen, …, J. A. Bouwstra. 2013. Localization of cholesterol and fatty acid in a model lipid membrane: a neutron diffraction approach. *Biophys. J.* 105:911–918.

24. Mojumdar, E. H., Z. Kariman, …, J. A. Bouwstra. 2014. The role of ceramide chain length distribution on the barrier properties of the skin lipid membranes. *Biochim. Biophys. Acta.* 1838:2473–2483.
25. Akinshina, A., C. Das, and M. G. Noro. 2016. Effect of monoglycerides and fatty acids on a ceramide bilayer. *Phys. Chem. Chem. Phys.* 18:17446–17460.
26. Das, C., M. G. Noro, and P. D. Olmsted. 2009. Simulation studies of stratum corneum lipid mixtures. *Biophys. J.* 97:1941–1951.
27. Das, C., M. G. Noro, and P. D. Olmsted. 2013. Lamellar and inverse micellar structures of skin lipids: effect of templating. *Phys. Rev. Lett.* 111:148101.
28. Das, C., M. G. Noro, and P. D. Olmsted. 2014. Fast cholesterol flip-flop and lack of swelling in skin lipid multilayers. *Soft Matter.* 10:7346–7352.
29. Guo, S., T. C. Moore, …, C. McCabe. 2013. Simulation study of the structure and phase behavior of ceramide bilayers and the role of lipid head group chemistry. *J. Chem. Theory Comput.* 9:5116–5126.
30. Gupta, R., B. S. Dwadasi, and B. Rai. 2016. Molecular dynamics simulation of skin lipids: effect of ceramide chain lengths on bilayer properties. *J. Phys. Chem. B.* 120:12536–12546.
31. Gupta, R., and B. Rai. 2015. Molecular dynamics simulation study of skin lipids: effects of the molar ratio of individual components over a wide temperature range. *J. Phys. Chem. B.* 119:11643–11655.
32. Hoopes, M. I., M. G. Noro, …, R. Faller. 2011. Bilayer structure and lipid dynamics in a model stratum corneum with oleic acid. *J. Phys. Chem. B.* 115:3164–3171.
33. Imai, Y., X. Liu, …, T. Hoshino. 2010. Computational analysis of water residence on ceramide and sphingomyelin bilayer membranes. *J. Mol. Graph. Model.* 29:461–469.
34. Notman, R., J. Anwar, …, W. K. den Otter. 2008. Simulations of skin barrier function: free energies of hydrophobic and hydrophilic transmembrane pores in ceramide bilayers. *Biophys. J.* 95:4763–4771.
35. Notman, R., W. K. den Otter, …, J. Anwar. 2007. The permeability enhancing mechanism of DMSO in ceramide bilayers simulated by molecular dynamics. *Biophys. J.* 93:2056–2068.
36. Paloncýová, M., R. H. DeVane, …, M. Otyepka. 2014. Rationalization of reduced penetration of drugs through ceramide gel phase membrane. *Langmuir.* 30:13942–13948.
37. Paloncýová, M., K. Vávrová, …, K. Berka. 2015. Structural changes in ceramide bilayers rationalize increased permeation through stratum corneum models with shorter acyl tails. *J. Phys. Chem. B.* 119:9811–9819.
38. Pandit, S. A., and H. L. Scott. 2006. Molecular-dynamics simulation of a ceramide bilayer. *J. Chem. Phys.* 124:14708.
39. Uppulury, K., P. S. Coppock, and J. T. Kindt. 2015. Molecular simulation of the DPPE lipid bilayer gel phase: coupling between molecular packing order and tail tilt angle. *J. Phys. Chem. B.* 119:8725–8733.
40. Sparr, E., L. Eriksson, …, K. Ekelund. 2001. AFM study of lipid monolayers: III. Phase behavior of ceramides, cholesterol and fatty acids. *Langmuir.* 17:164–172.
41. Školová, B., K. Hudská, …, K. Vávrová. 2014. Different phase behavior and packing of ceramides with long (C16) and very long (C24) acyls in model membranes: infrared spectroscopy using deuterated lipids. *J. Phys. Chem. B.* 118:10460–10470.
42. Oguri, M., G. S. Gooris, …, J. A. Bouwstra. 2014. The effect of the chain length distribution of free fatty acids on the mixing properties of stratum corneum model membranes. *Biochim. Biophys. Acta.* 1838:1851–1861.
43. Klauda, J. B., R. M. Venable, …, R. W. Pastor. 2010. Update of the CHARMM all-atom additive force field for lipids: validation on six lipid types. *J. Phys. Chem. B.* 114:7830–7843.
44. Gillams, R. J., J. V. Busto, …, S. E. McLain. 2015. Solvation and hydration of the ceramide headgroup in a non-polar solution. *J. Phys. Chem. B.* 119:128–139.
45. Gillams, R. J., C. D. Lorenz, and S. E. McLain. 2016. Comparative atomic-scale hydration of the ceramide and phosphocholine headgroup in solution and bilayer environments. *J. Chem. Phys.* 144:225101.
46. Jorgensen, W. L., J. Chandrasekhar, …, M. L. Klein. 1983. Comparison of simple potential functions for simulating liquid water. *J. Chem. Phys.* 79:926.
47. Marinari, E., and G. Parisi. 1992. Simulated tempering: a new Monte Carlo scheme. *Europhys. Lett.* 19:451–458.
48. Abraham, M. J., T. Murtola, …, E. Lindahl. 2015. Gromacs: high performance molecular simulations through multi-level parallelism from laptops to supercomputers. *SoftwareX.* 1–2:19–25.
49. Hoover, W. G. 1985. Canonical dynamics: equilibrium phase-space distributions. *Phys. Rev. A Gen. Phys.* 31:1695–1697.
50. Parrinello, M., and A. Rahman. 1981. Polymorphic transitions in single crystals: a new molecular dynamics method. *J. Appl. Phys.* 52:7182–7190.
51. Essmann, U., L. Perera, …, L. G. Pedersen. 1995. A smooth particle mesh Ewald method. *J. Chem. Phys.* 103:8577–8593.
52. Das, C., P. D. Olmsted, and M. G. Noro. 2009. Water permeation through stratum corneum lipid bilayers from atomistic simulations. *Soft Matter.* 5:4549.
53. Hartkamp, R., T. C. Moore, …, C. McCabe. 2016. Investigating the structure of multicomponent gel-phase lipid bilayers. *Biophys. J.* 111:813–823.
54. Gunstone, F. D., J. L. Harwood, and F. B. Padley. 1994. The Lipid Handbook. Chapman and Hall, London, United Kingdom.
55. Boughter, C. T., V. Monje-Galvan, …, J. B. Klauda. 2016. Influence of cholesterol on phospholipid bilayer structure and dynamics. *J. Phys. Chem. B.* 120:11761–11772.
56. Shieh, H. S., L. G. Hoard, and C. E. Nordman. 1977. Crystal structure of anhydrous cholesterol. *Nature.* 267:287–289.
57. Tieleman, D. P., and H. J. C. Berendsen. 1996. Molecular dynamics simulations of a fully hydrated dipalmitoylphosphatidylcholine bilayer with different macroscopic boundary conditions and parameters. *J. Chem. Phys.* 105:4871–4880.

Biophysical Journal, Volume *114*

Supplemental Information

Effect of Ceramide Tail Length on the Structure of Model Stratum Corneum Lipid Bilayers

Timothy C. Moore, Remco Hartkamp, Christopher R. Iacovella, Annette L. Bunge, and Clare M^{c}Cabe

1 Random Walk Molecular Dynamics

Figure S1 shows a representative temperature walk taken during the RWMD simulations. Note that for the first $25\,\mathrm{ns}$, the temperature (randomly) oscillates between $305\,\mathrm{K}$ and $355\,\mathrm{K}$, and that the upper temperature limit linearly reduces to $305\,\mathrm{K}$ during the final $25\,\mathrm{ns}$.

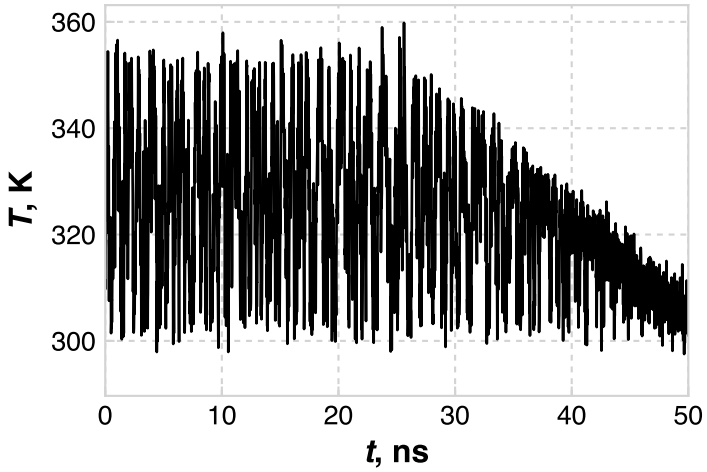

Figure S1: A representative plot of temperature versus time during the RWMD simulation.

2 Analysis

The area per lipid (APL) is taken to be the cross-sectional area of the simulation box divided by the number of lipids in each leaflet. The tilt angle of the lipid tails is defined as the average angle between the long axis of each lipid tail and the z-axis. The long axis of a lipid tail is defined by the eigenvector corresponding to the minimum eigenvalue of the inertia tensor, which is calculated from the positions and masses of the atoms in the lipid tail. We define two tails for CER NS, the fatty acid tail (which varies in length in this work), and the sphingosine tail. We define the FA tail as the alpha carbon on the FA tail plus the next 14 carbons, and their associated hydrogens. Note that this corresponds to the entire FA tail of eCER, but neglects the terminal 8 carbons of the uCER FA tail so as to remove the influence of the low tail density region on the inertia tensor. The sphingosine tail is defined as the terminal 13 carbons of the sphingosine tail (i.e., all carbons beyond the double bond), and is the same for eCER and uCER. CHOL is treated as a single tail, and the terminal 8 carbons of FFA are neglected in the inertia calculation. The area per tail (APT) is defined as the cross-sectional area of the simulation box divided by the number of tails in each leaflet (2 for CER, 1 for CHOL and FFA), multiplied by the cosine of the tilt angle to map the area into a plane perpendicular to the lipid tails. The nematic order parameter, which provides a measure of the global order of the lipid tails, was calculated as in Ref. S1. Briefly, the long axes of the lipid tails in each leaflet are used to construct the nematic tensor of the system, and the nematic order parameter is the largeset eigenvalue of this nematic tensor. Note that for systems that have a small population of CHOL lying at the middle of the bilayer, the CHOL molecules at the center of the bilayer were not included in the APL, APT, tilt angle, or nemtaic order parameter calculations.

The neutron scattering length density profiles were calculated by constructing a histogram of the lipid atom positions, weighted by the bound coherent neutron scattering lengths of each element. The bound coherent neutron scattering lengths were taken from `http://www.ati.ac.at/~neutropt/scattering/ScatteringLengthsAdvTable.pdf`.

The density profile of water is used to calculate the bilayer thickness, as in Ref. S2. The bilayer thickness is calculated as the distance between the lipid-water interfaces on each side of the bilayer, which is defined as the z value where the water density is $1/e$ of the bulk value. A schematic of this calculation is shown in Figure S2. Similarly, the width of the interfacial region is defined as the range in z where the water density goes from the bulk value to $1/e$ of the bulk value. This region is also shown in Figure S2.

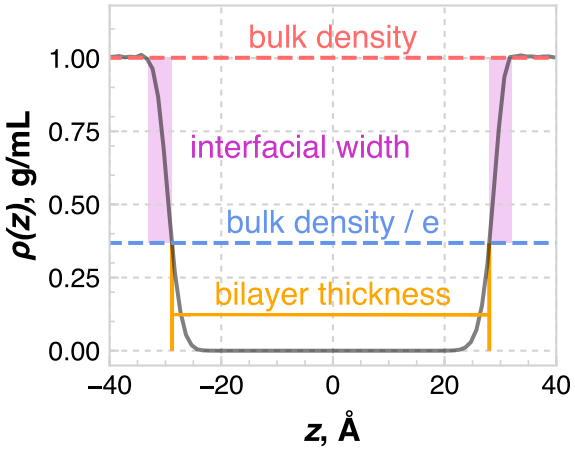

Figure S2: Schematic of the bilayer thickness calculation. The gray line is the water density profile across the bilayer, from which the bulk value is calculated. The intersection of the water density profile and the $\rho = \rho_{bulk}/e$ defines the edges of the bilayer. The width of the lipid-water interface is shown as the width of the purple rectangles.

The low tail density region of the bilayer is defined as the region in the middle of the bilayer where the density is below that of the plateau region of high tail density, as shown in Figure S3.

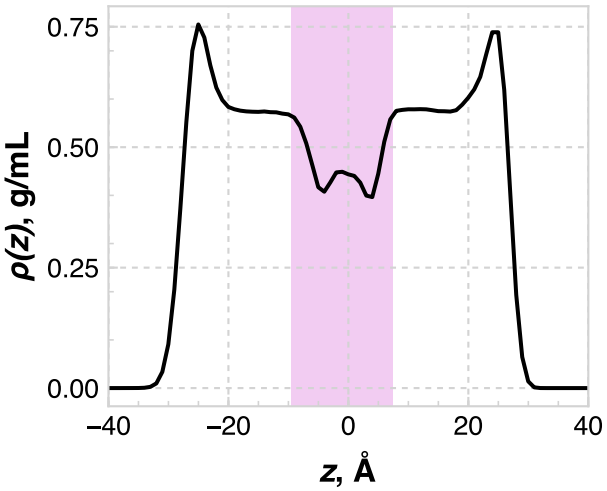

Figure S3: Visualization of the low tail density region, as calculated from the total lipid mass density profile, shown as the purple rectangle. This example is for the pure CER NS bilayer with a 1:3 eCER:uCER ratio.

The coordination numbers (CNs), which were used to describe the lateral distributions of lipid species, were calculated as the make up of the 6 nearest lipid tails for a given tail type, e.g., the CHOL-CHOL CN describes how many CHOL molecules are in the 6 nearest neighbors of each CHOL. The 6 nearest neighbors were used since the lipid tails are found to pack on a hexagonal lattice. The position of each tail in a bilayer leaflet is taken as the center of mass of the tail projected into the plane $z = 0$. As with the APL, APT, tilt angle, and nematic order parameter, any CHOL molecules at the center of the bilayer were neglected in the calculation of the coordination numbers.

The lipid backbone orientations were calculated to quantify the rotational motion of the lipids in the bilayer plane. The backbone orientation was taken to be the vector pointing from the 3rd carbon on the sphingosine tail to the α-carbon of the fatty acid tail. The x and y components of of this vector through time ($x(t)$ and $y(t)$, respectively), were used to calculate the rotational autocorrelation function by:

$$C(t) = \left\langle \frac{x(t)x(0) + y(t)y(0)}{[x(0)]^2 + [y(0)]^2} \right\rangle,$$

where the angle brackets denote an average over all CER NS molecules and multiple time origins. By using the x and y components, rather than the angle with respect to an arbitrary vector in the bilayer plane, the sensitivity to values near $0°$ is removed (e.g., $0°$ and $359°$ are very similar physically, but not mathematically).

The hydrogen bonding is determined with geometric criteria, following the work of Ferrario et al. (S3): a hydrogen bond between a donor-hydrogen-acceptor set is said to exist if the donor-acceptor distance $r_{DA} \leq 3.5$ Å, the hydrogen-acceptor distance $r_{HA} \leq 2.6$ Å, and the hydrogen-aceptor-donor angle $\angle HAD < 30°$. Nitrogen and oxygen are considered potential hydrogen bond acceptors, and hydrogen-donor pairs consist of a nitrogen or an oxygen bonded to a hydrogen.

3 Structural Properties

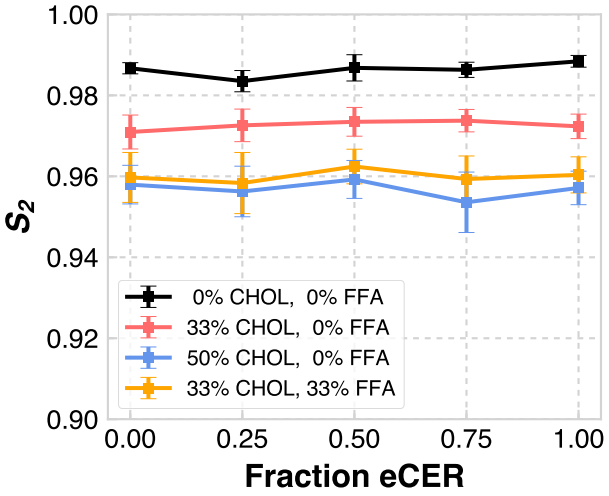

Figure S4: Nematic order parameter S_2 of the systems considered in this study. Note that the abscissa gives the fraction of CER NS that is eCER, not the total fraction of eCER in the system.

Table 1: Nematic order parameter of the lipid tails as a function of lipid composition.

	fraction eCER				
CER NS:CHOL:FFA	0.0	0.25	0.5	0.75	1.0
1:0:0	0.987	0.984	0.987	0.986	0.988
2:1:0	0.971	0.973	0.973	0.974	0.972
1:1:0	0.958	0.956	0.959	0.954	0.957
1:1:1	0.960	0.958	0.962	0.959	0.960

Table 2: Bilayer thickness (in Å) as a function of bilayer composition.

	fraction eCER				
CER NS:CHOL:FFA	0.0	0.25	0.5	0.75	1.0
1:0:0	56.8	54.3	52.5	48.1	45.1
2:1:0	51.4	50.5	47.2	44.3	42.6
1:1:0	47.8	45.7	44.7	43.1	40.3
1:1:1	51.8	51.5	49.0	47.8	47.3

Table 3: Thickness of the lipid-water interface (in Å) as a function of lipid composition.

	fraction eCER				
CER NS:CHOL:FFA	0.0	0.25	0.5	0.75	1.0
1:0:0	4.2	4.9	5.0	4.6	3.6
2:1:0	4.7	4.6	4.7	4.9	4.2
1:1:0	5.2	5.2	5.7	4.8	4.7
1:1:1	5.0	5.7	5.2	5.2	5.0

Table 4: Hydrogen bonds between lipid components for the ternary system with a 1:1 eCER:uCER ratio.

	eCER	**uCER**	**CHOL**	**FFA**
eCER	2.2	2.9	4.3	1.4
uCER	2.9	1.5	3.7	1.1
CHOL	4.3	3.7	0.0	0.7
FFA	1.4	1.1	0.7	1.0

Table 5: Hydrogen bonds between lipid components for the 2:1 CER NS:CHOL system with a 1:1 eCER:uCER ratio.

	eCER	**uCER**	**CHOL**
eCER	7.3	12.1	6.4
uCER	12.1	6.9	5.0
CHOL	6.4	5.0	0.0

Table 6: Hydrogen bonds between lipid components for the 1:1 CER NS:CHOL system with a 1:1 eCER:uCER ratio.

	eCER	**uCER**	**CHOL**
eCER	5.2	5.8	6.0
uCER	5.8	5.7	5.1
CHOL	6.0	5.1	0.1

Table 7: CHOL-CHOL coordination numbers (i.e., the data from Figure S8).

	fraction eCER				
CER NS:CHOL:FFA	0.0	0.25	0.5	0.75	1.0
2:1:0	1.0	1.1	1.2	1.3	1.3
1:1:0	2.0	2.1	2.0	1.9	2.1
1:1:1	1.5	1.6	1.4	1.4	1.4

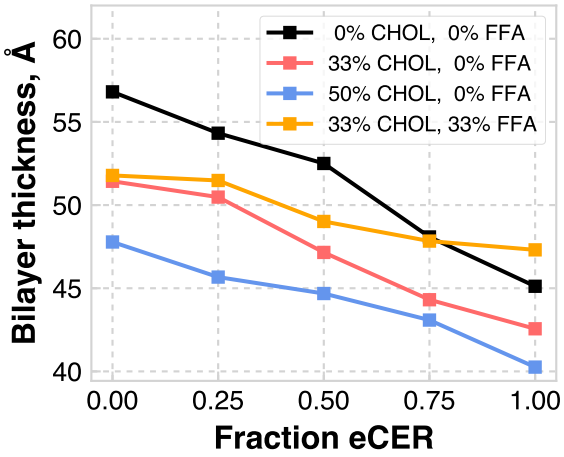

Figure S5: Bilayer thickness, as calculated from the water density profile, as a function of system composition.

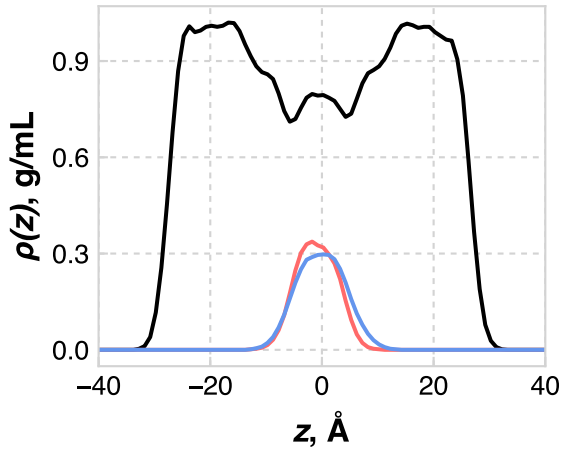

Figure S6: Density profiles of all lipids (black line), the unequal part of the uCER tail (red line), and the terminal 8 carbons of the FFA tail (blue line) for the equimolar uCER-CHOL-FFA system.

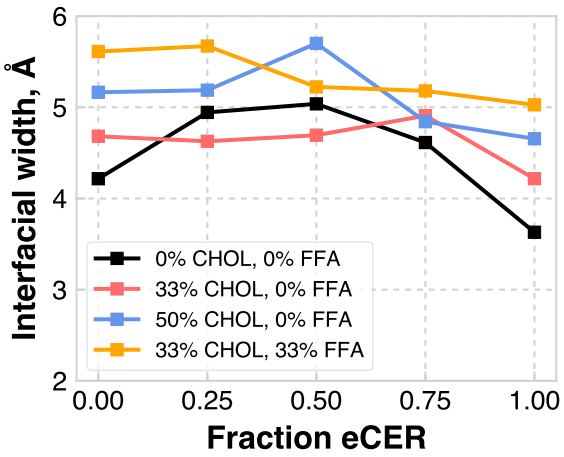

Figure S7: Thickness of the lipid-water interface for each system considered. Note that the abscissa gives the fraction of CER NS that is eCER, not the total fraction of eCER in the system.

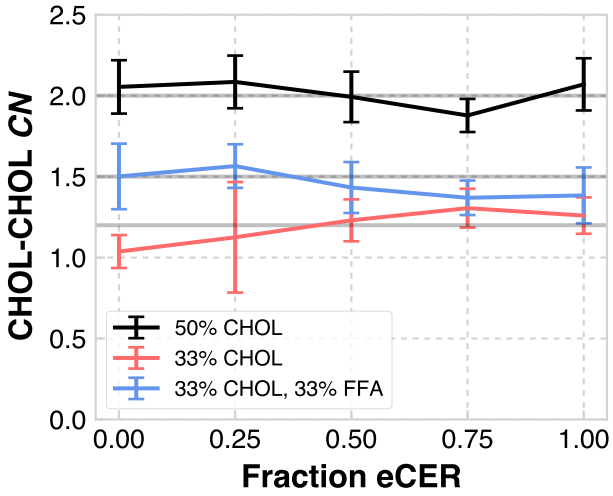

Figure S8: CHOL-CHOL coordination number (CN) as a function of composition and eCER fraction. The light gray lines represent the CN value for random mixing in the bilayer plane.

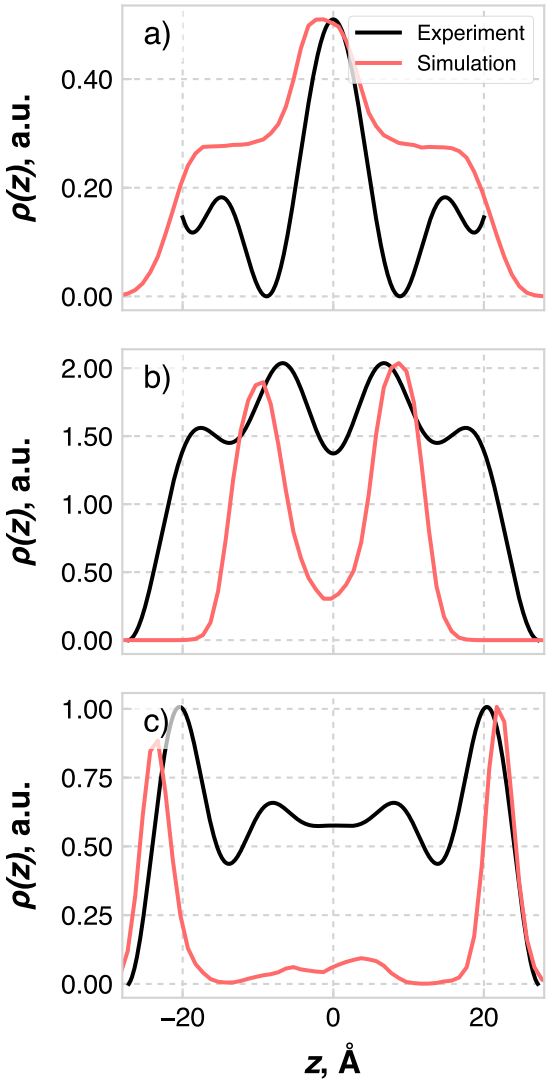

Figure S9: Localization of different components calculated via neutron diffraction on selectively deuterated lipid samples (experiment) and from this work (simulation). a) uCER FA tail; b) CHOL tail; c) CHOL headgroup. Experimental curves reproduces from Refs. S4 (a) and S5 (b, c). Note that the curves were shifted such that the minima lie at $\rho = 0$ and scaled to have the same height.

References

S1. Guo, S., T. C. Moore, C. R. Iacovella, L. A. Strickland, and C. McCabe, 2013. Simulation study of the structure and phase behavior of ceramide bilayers and the role of lipid headgroup chemistry. Journal of Chemical Theory and Computation 9:5116–5126.

S2. Das, C., M. G. Noro, and P. D. Olmsted, 2009. Simulation studies of stratum corneum lipid mixtures. Biophysical Journal 97:1941–1951.

S3. Ferrario, M., M. Haughney, I. R. McDonald, and M. L. Klein, 1990. Molecular-dynamics simulation of aqueous mixtures: Methanol, acetone, and ammonia. The Journal of Chemical Physics 93:5156–5166.

S4. Groen, D., G. Gooris, D. Barlow, M. Lawrence, J. Van Mechelen, B. Demé, and J. Bouwstra, 2011. Disposition of ceramide in model lipid membranes determined by neutron diffraction. Biophysical Journal 100:1481–1489.

S5. Mojumdar, E., D. Groen, G. Gooris, D. Barlow, M. Lawrence, B. Deme, and J. Bouwstra, 2013. Localization of cholesterol and fatty acid in a model lipid membrane: a neutron diffraction approach. Biophysical Journal 105:911–918.